

CrystEngComm

Accepted Manuscript



This is an *Accepted Manuscript*, which has been through the Royal Society of Chemistry peer review process and has been accepted for publication.

Accepted Manuscripts are published online shortly after acceptance, before technical editing, formatting and proof reading. Using this free service, authors can make their results available to the community, in citable form, before we publish the edited article. We will replace this *Accepted Manuscript* with the edited and formatted *Advance Article* as soon as it is available.

You can find more information about *Accepted Manuscripts* in the [Information for Authors](#).

Please note that technical editing may introduce minor changes to the text and/or graphics, which may alter content. The journal's standard [Terms & Conditions](#) and the [Ethical guidelines](#) still apply. In no event shall the Royal Society of Chemistry be held responsible for any errors or omissions in this *Accepted Manuscript* or any consequences arising from the use of any information it contains.



Exposed Facets and Crystal Phases Tuning of Tungsten Oxide Hierarchical Nanostructures and Their Enhanced Visible-Light-Driven Photocatalytic Performance

Received 00th January 20xx,
Accepted 00th January 20xx

DOI: 10.1039/x0xx00000x

www.rsc.org/

Yesheng Li,^a Zilong Tang,^{*a} Junying Zhang^{*,b} and Zhongtai Zhang^a

Tungsten oxide hierarchical nanostructures controllably assembled with one dimensional nanosized building blocks which exhibit different exposed facets and crystal phases were synthesized via a facile hydrothermal reaction assisted by urea. Systematic and comprehensive investigations indicate that urea plays a significant role in tuning facets exposure of building blocks and controlling crystal phase by effectively regulating the process of nucleation. Adjusting the amount of urea can obtain proper crystal phase and tune exposed facets to achieve highest photocatalytic activity of tungsten oxide. It has been found that (020) is the active facet of orthorhombic $\text{WO}_3 \cdot 0.33\text{H}_2\text{O}$ but not for hexagonal WO_3 . The orthorhombic $\text{WO}_3 \cdot 0.33\text{H}_2\text{O}$ exposing most (020) facets shows highest photocatalytic activity for the degradation of rhodamine B under visible light illumination, 4.1 times as high as that of the sample exposing least (020) facets.

1. Introduction

Tungsten oxides have been widely studied owing to their potential applications as catalysts, gas sensors, electrochromic and optochromic devices. Especially, tungsten oxide nanocrystals are a system of particular interest for the study of photocatalysis, as tungsten oxide is stable under a wide range of conditions and has a band gap of 2.5–2.8 eV, which is ideal for absorption of visible light.¹ Furthermore, tungsten oxides has a moderate hole diffusion length (~150 nm) compared with $\alpha\text{-Fe}_2\text{O}_3$ (2–4 nm) and TiO_2 (10^4 nm) and inherently good electron transport properties.^{1,2} Therefore, tungsten oxides have been thought to be promising visible-light-driven photocatalysts in solar energy conversion and environmental remediation. Many efforts have been devoted to improve the photocatalytic performance of photocatalyst including use of macro/mesoporous structures,^{3–5} crystal facet engineering,^{6,7} metal and non-metal doping,^{8,9} and three-dimensional (3D) hierarchical structures.^{10,11} Among these, 3D hierarchical structures forming via low-dimensional nanosized building block assembly have attracted more attention since 3D hierarchical structures can provide numerous active sites because of their low density, high surface area, easy settlement, good delivering ability, and surface permeability,¹² resulting in the improvement in photocatalytic performance. Therefore, it is essential to develop facile approaches to synthesizing 3D hierarchical structures in a controlled fashion.

Fabrication of 3D structure of tungsten oxides at the microscopic and controllable level is still a significant challenge.

At present, the design and morphological control of the crystal facets is considered to be a hot spot in scientific research. Many applications such as heterogeneous catalysis, gas sensing, and solar-energy conversion are very sensitive to the surface structures on an atomic level.^{13–19} Abundant references have reported the determinant effects of exposing facets on the performance of TiO_2 , and various samples synthesis methods have been proposed.^{7,13,15,20} The photocatalytic activities dependence on the exposed facets of tungsten oxides has been preliminarily investigated.^{18,19,21–29} It was reported that the surface energy of crystal faces in WO_3 nanocrystals with monoclinic crystal structure follow the order (002) > (020) > (200).²¹ Massimiliano *et al.*²² demonstrated that (020) and (002) crystal surfaces provided privileged reactive sites for ammonia oxidation and therefore they played a key role in driving the sensing properties of monoclinic WO_3 layers. Li *et al.*²⁵ found that the degree of exposure of (010) facet in orthorhombic $\text{WO}_3 \cdot n\text{H}_2\text{O}$ samples correlated well with the measured photocatalytic activities. Jia *et al.*²⁷ indicated that WO_3 samples with hexagonal structure exposed (002) facets exhibited better acetone sensitivity and selectivity than those exposed (100) facets. As for triclinic WO_3 nanoparticles exposing (001), (100) and (010) facets, it was suggested that (010) was the most active facet.²⁹ As mentioned above, many properties are strongly dependent on the exposed planes. Simultaneously, the exposed facets also have tight relationships with the crystal phase which they belong to. However, the crystallographic orientation and crystal phase dependence of tungsten oxides' photocatalytic activity still has not been well established or systematically studied. Therefore, it is essential to develop facile approaches to synthesizing tungsten oxides with tunable exposed facets and crystal phases.

^a State Key Laboratory of New Ceramics and Fine Processing, School of Materials Science and Engineering, Tsinghua University, Beijing 100084, China. Email: tzl@tsinghua.edu.cn; Fax: +86 10 62771160

^b Department of Physics, Beihang University, Beijing 100191, China. Email: zjy@buaa.edu.cn; tel: +86 10 82315351

[†] Electronic Supplementary Information (ESI) available. See DOI: 10.1039/b000000x/

In this work, the 3D tungsten oxide hierarchical nanostructures with different exposed facets and crystal phases have been successfully obtained via hydrothermal reaction assisted by urea. Adjusting the amount of urea can cause the crystal structure transformation from orthorhombic $\text{WO}_3 \cdot 0.33\text{H}_2\text{O}$ to hexagonal WO_3 . Meanwhile, the 3D tungsten oxides hierarchical nanostructures building blocks vary from nanobricks via nanorods and nanoflakes and finally to nanobelts, changing the exposed facets. The mechanism of phase-control and exposed facets-control by urea was carefully investigated. It is indicated that the two NH proton donors and C=O proton acceptor enable urea to insert into the layers of tungsten hydrates and the weak basicity allows it to cause the change of pH values during hydrothermal reaction through hydrolysis, thereby realizing phase-control and exposed facets-control. Meanwhile, it is found that (020) is the most active facet of orthorhombic $\text{WO}_3 \cdot 0.33\text{H}_2\text{O}$ but not for hexagonal WO_3 . Thus, $o\text{-WO}_3 \cdot 0.33\text{H}_2\text{O}$ exposing the active (020) facet achieves higher photocatalytic activities than $h\text{-WO}_3$ exposing almost all (020) facet.

2. Experimental

2.1. Synthesis of tungsten oxides with hierarchical nanostructures

All the chemicals (Sinopharm Chemical Reagent Co., Ltd) were of analytical reagent grade and used without further purification. All the aqueous solutions were prepared using deionized water.

Tungsten oxides with hierarchical nanostructures were synthesized through hydrothermal reaction by using urea as additives. In a typical process, 0.875 g tungstic acid was added into 18 mL H_2O_2 , stirred at 90 °C for 1.5 h before converting into a transparent sol. The resulting clear sol was diluted using deionized water to 210 mL, and then the as-prepared solution was added 14 mL 3 M HCl. After stirring for another 20 min, 30 mL of the precursor solution was transferred into a 50 mL Teflon-lined autoclave followed by adding a certain amount of urea. Finally, the autoclave was sealed and maintained at 180 °C for 12 h. The as-synthesized precipitate was washed with deionized water for many times, and then dried in vacuum at 80 °C for 3 h. The samples which were obtained using 0 g, 0.036 g, 0.072 g, 0.144 g and 0.180 g urea were labeled as WU0, WU1, WU2, WU3 and WU4.

2.2. photocatalytic activity measurement

Photocatalytic properties of the samples were evaluated by measuring the concentration of rhodamine B (RhB) in aqueous solution after equilibration in dark and irradiating with visible-light achieved from a 300 W Xenon lamp by a cutoff filter ($\lambda > 400$ nm). Typically, 20 mg sample was dispersed in 40 mL RhB aqueous solution (15 mg L^{-1}). Before the samples were exposed to visible light irradiation, the suspension was stirred over night to ensure the equilibrium of dye adsorption on the surfaces of the samples. About 3 mL of the solution was taken every 20 min during the photocatalysis, and the powder sample was separated from the solution via centrifugation and the RhB concentration was measured by UV-Vis spectroscopy.

2.3. Characterization of materials

Crystallographic structures of the as-prepared materials were characterized by power X-ray diffraction (XRD, Cu $\text{K}\alpha$, Rigaku D/max-V2500, Japan) from 10° to 70° (2 θ) at 8° min^{-1} . Particle sizes, morphologies and microstructures were studied by scanning electron microscopy (SEM, ZEISS, Germany) and transmission electron microscopy (TEM, JEOL-2011, Japan and HT7700, Japan). UV/Vis absorption spectra were recorded with UV-Vis spectrophotometer (U-3010, Hitachi, Japan). The X-ray photoelectron spectroscopy (XPS) were determined on an ESCALAB 250Xi instrument (Thermo Fisher Scientific, USA). The surface areas of the samples were measured by the Brunauer-Emmett-Teller (BET) method using nitrogen adsorption-desorption isotherms at 77 K with a Contador QuadraSorb SI-MP instrument. The Raman spectra were recorded by high-resolution Raman spectroscopy (HR800, HORIBA JOBIN YVON, France). Electron spin resonance spectroscopy (ESR) measurements were performed at room temperature with a JEOL FA200 ESR spectrometer under UV light or visible light irradiation.

3. Results and discussion

3.1. Structure and morphology

The XRD patterns of the tungsten oxides prepared under different conditions are presented in Fig. 1. The main peaks are very strong and narrow, indicating that the samples exhibit high crystallographic quality. All the peaks of the samples WU0, WU1, WU2 and WU3 are indexed to orthorhombic structure of $\text{WO}_3 \cdot 0.33\text{H}_2\text{O}$ ($o\text{-WO}_3 \cdot 0.33\text{H}_2\text{O}$) (JCPDS no. 72-0199), as shown in Fig. 1. Sample WU4 yields a hexagonal WO_3 phase ($h\text{-WO}_3$), with the XRD patterns corresponding to JCPDS no. 85-2460. Besides, pure $o\text{-WO}_3 \cdot 0.33\text{H}_2\text{O}$ was obtained when the mass of urea was below 0.162 g, while the product turned into pure $h\text{-WO}_3$ after adding a little more urea (4 mg) as shown Fig. S1, suggesting that there may exist a critical concentration of urea for phase transition. In short, a high concentration of urea results in pure $h\text{-WO}_3$ phase, otherwise, $o\text{-WO}_3 \cdot 0.33\text{H}_2\text{O}$ phase will appear. Besides, a gradual increase in the relative intensity is observed for the (020) diffraction peak on going from WU0 to WU3 and the intensities of (100) and (200) diffraction peaks for sample WU4 is much stronger than (020) diffraction peak of all the other four samples, suggesting that adjusting the amount of urea may tune different facets exposure. To sum up, through adjusting the amount of urea, the crystal structure of tungsten oxides could be controlled.

Fig. 2 displays the UV-Vis absorbance spectra of the samples prepared with different amounts of urea. It indicates a red shift tendency in the absorption upon increasing urea. When adding a small amount of urea (WU1), the light absorption remains unchanged compared with WU0 and when increasing the amount of urea (WU2 and WU3), the light absorption intensity in the visible-light region (450-800 nm) is slightly increased. Moreover, when the crystal phase of the sample transforms to $h\text{-WO}_3$ (WU4), the light absorption intensity in the visible-light region is enhanced compared with WU0 and the absorption edge shifts to 480 nm.

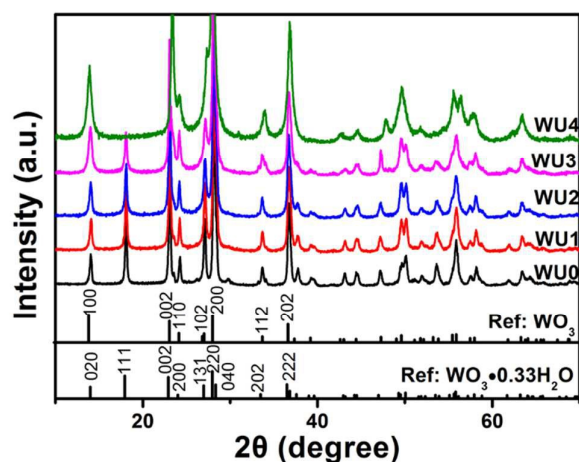


Fig. 1 XRD patterns of the tungsten oxides power prepared with different amounts of urea: 0 g (WU0), 0.036 g (WU1), 0.072 g (WU2), 0.144 g (WU3) and 0.180 g (WU4)

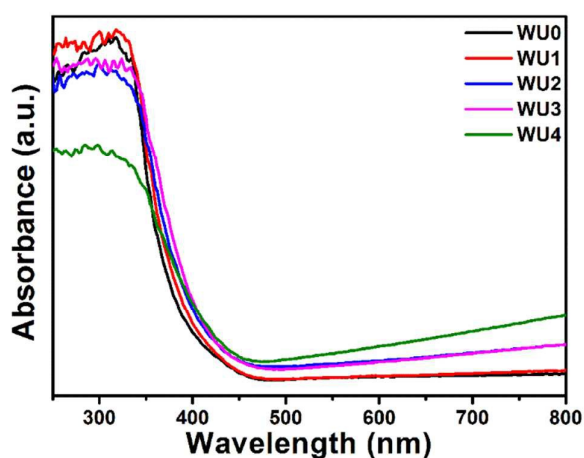


Fig. 2 UV-Vis absorbance spectra of samples obtained with different amounts of urea.

The SEM images of the samples prepared with different amounts of urea are shown in Fig. 3. Fig. 3a presents that when urea is absent, the sample WU0 has a uniform flower-like shape with a diameter about 1-2 μm and assembled with many very thick and big rectangle cross-section nanobricks. As can be seen in Fig. 3b, when adding a low amount (0.036 g) of urea, the sample displays numerous thinner nanorods but still contains a lot of big nanobricks. As the amount of urea increases, the big nanobricks disappear gradually and finally only regular microspheres composed of ultrathin nanowires are obtained (shown in Fig. 3c-3f). Besides, it is noticed that the $o\text{-WO}_3\cdot 0.33\text{H}_2\text{O}$ phase (WU0, WU1, WU2 and WU3) maintains hierarchical nanostructures assembled with cuboid-like block buildings, although the size of block buildings decreases as the amount of urea increases. However, when $h\text{-WO}_3$

phase exists in the sample (WU4) the hierarchical nanostructures assembled with ultrathin nanowires appear. These morphology variation can be reflected from the specific surface area of the as-prepared samples. The samples prepared with increasing the amount of urea show specific surface area of 12.5, 18.2, 20.6, 21.4 and $80.6\text{ m}^2\text{g}^{-1}$, suggesting a tendency to increase. Besides, the specific surface area has a dramatic increase when the $o\text{-WO}_3\cdot 0.33\text{H}_2\text{O}$ transforms into $h\text{-WO}_3$, corresponding to the morphology change from nanorods to ultrathin nanowires. And similarly, the morphology has a significant change between adding 0.162 g urea and 0.166 g urea (Fig. S1b and S1c). Above all, the evolution of morphology has a significant relationship with the evolution of crystal phase and adjustable morphology would be acquired by controlling the amount of urea.

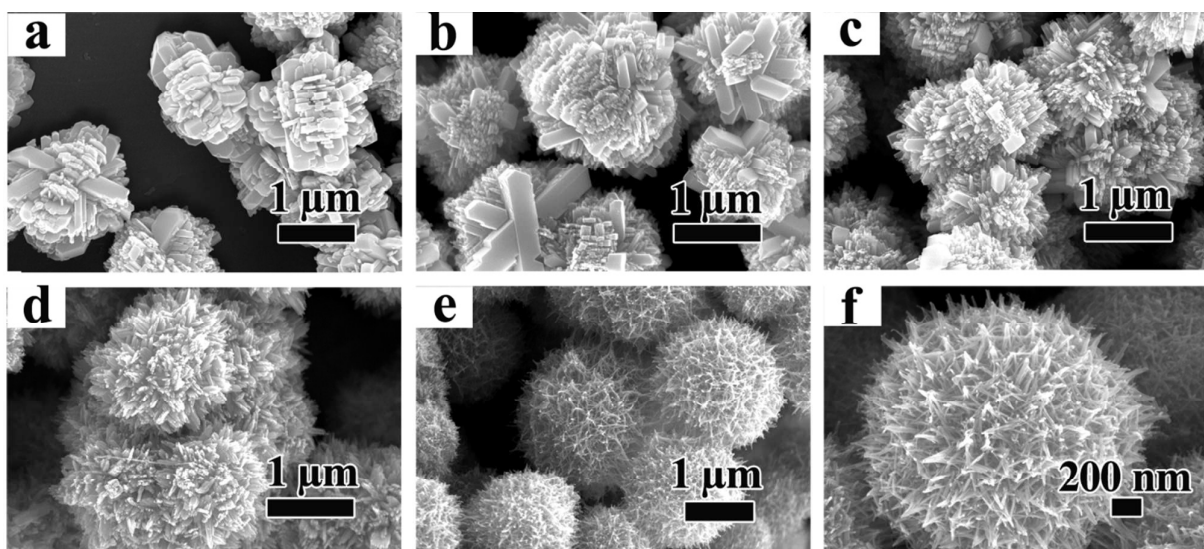


Fig. 3 SEM images of the as-prepared tungsten oxides with different amounts of urea: (a) 0 g (WU0); (b) 0.036 g (WU1); (c) 0.072 g (WU2); (d) 0.144 g (WU3); (e) 0.180 g (WU4) and its corresponding enlarged picture (f).

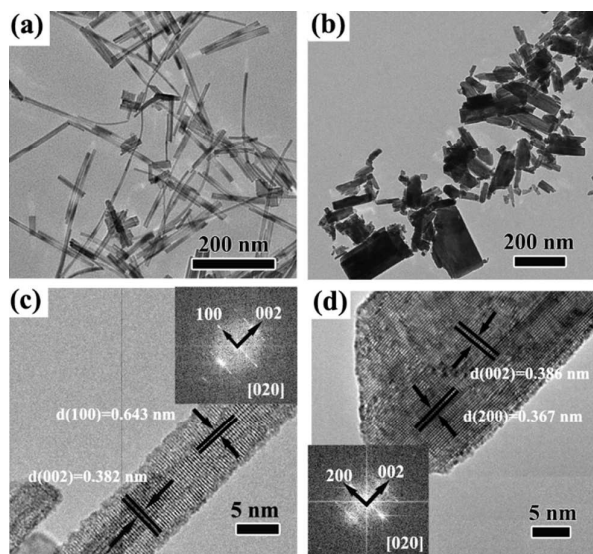


Fig. 4 TEM and HRTEM images for h- WO_3 crystal (a, c) and o- $\text{WO}_3 \cdot 0.33\text{H}_2\text{O}$ crystal (b, d) and their corresponding FFT spots (inserts)

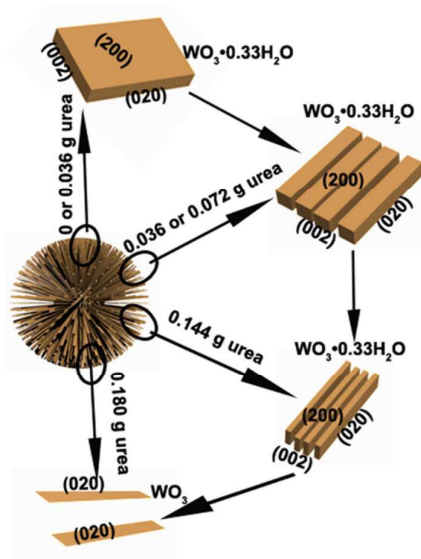


Fig. 5 Schematic illustration of the building blocks.

From the above results, we can confirm that the sample composes pure h- WO_3 phase or o- $\text{WO}_3 \cdot 0.33\text{H}_2\text{O}$ phase. Further information on the microstructure of h- WO_3 and o- $\text{WO}_3 \cdot 0.33\text{H}_2\text{O}$ is obtained from TEM images and high resolution transmission electron microscopy (HRTEM) images in Fig. 4. Fig. 4a and 4c show

that WU4 microsphere is assembled by nanobelts rather than nanowires. The nanobelts almost have one exposed facet and have a uniform width of 6-7 nm and a length of several hundred nanometers. The spacing of the lattice fringes are found to be about 0.382 and 0.643 nm, as shown in Fig. 4c. These planes can be well indexed as (002) and (100) planes of the h- WO_3 crystal. The measurements of both interplanar spacing and FFT spots indicate that these two planes belong to [020] zone axis. Based on the above observations, it can be concluded that the length direction of h- WO_3 crystal nanobelts is along its [002] crystal orientation. For o- $\text{WO}_3 \cdot 0.33\text{H}_2\text{O}$ synthesized with 0.072 g urea (WU2), the morphology is quite different. Besides nanorods, some bigger nanobricks appear as shown in Fig. 4b. The lattice fringe spacings shown in Fig. 4d are 0.367 and 0.386 nm, which respectively correspond to the (200) and (002) interplanar spacing, confirmed by FFT spots in the inset of Fig. 4d. From the above analysis, the nanorods also grow along its [002] crystal orientation. To sum up, adjusting the amount of urea can tune the crystal structure transfer from orthorhombic $\text{WO}_3 \cdot 0.33\text{H}_2\text{O}$ to hexagonal WO_3 and the 3D tungsten oxides hierarchical nanostructures building blocks variation from nanobricks via nanorods and nanoflakes and finally to nanobelts. Actually, the evolution of morphology is just the variation of exposed facet. The vibration from exposing three facets (200), (020) and (002) to almost exposing one facet (020), suggests the increasing of (020), corresponding to the vibration of XRD patterns in Fig. 1. The schematic illustration of exposed facets evolution is shown in Fig. 5.

These variations in the size and exposed facets of building block and the crystal phase of tungsten oxides are also reflected in the XPS spectra and Raman spectra. In the high-resolution spectra of W 4f (Fig. 6a), there are two peaks at 35.7 and 37.8 eV for o- $\text{WO}_3 \cdot 0.33\text{H}_2\text{O}$ crystal which can be ascribed to W 4f_{7/2} and W 4f_{5/2}, respectively. These results signify that W is in the +6 oxidation state with the typical binding energies. Notably, the binding energy values of W 4f_{7/2} and W 4f_{5/2} in the h- WO_3 crystals (36.0 and 38.2 eV) are slightly positive shifted compared with those for o- $\text{WO}_3 \cdot 0.33\text{H}_2\text{O}$, which is perhaps attributed to size effect.³⁰⁻³² From SEM and TEM images above, the size of building block in the WO_3 hierarchical nanostructures is much smaller than that of o- $\text{WO}_3 \cdot 0.33\text{H}_2\text{O}$ hierarchical nanostructures, thus resulting in positive shift of the binding energy. The Raman spectra are shown in Fig. 6b. For the sample WU0 composed of pure o- $\text{WO}_3 \cdot 0.33\text{H}_2\text{O}$ phase, peaks centered at about 684 and 802 cm^{-1} are ascribed to neighboring oxygen atoms [$\nu(\text{O}-\text{W}-\text{O})$]. The peaks at around 917 and 946 cm^{-1} are attributed to the terminal $-\text{W}=\text{O}$ bonds, whereas those at around 215, 257 and 338 cm^{-1} arise from the $\text{O}-\text{W}-\text{O}$ bending modes [$\delta(\text{O}-\text{W}-\text{O})$]. The Raman spectra show that as the crystal phase transforms from o- $\text{WO}_3 \cdot 0.33\text{H}_2\text{O}$ to h- WO_3 and the building block changes from big nanobrick to ultrathin nanobelt, the

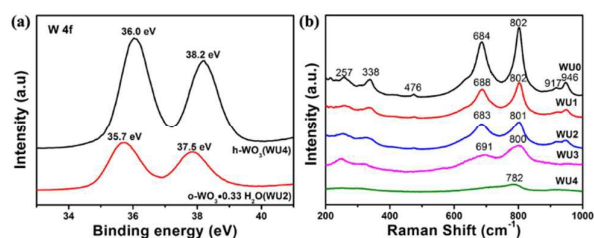


Fig. 6. (a) XPS spectra of W 4f of $o\text{-WO}_3 \cdot 0.33\text{H}_2\text{O}$ phase and $h\text{-WO}_3$ phase; (b) Raman spectra of the samples prepared by different amounts of urea

peak centered at about 800 cm^{-1} exhibits gradually blue shift and becomes broader and weaker. This phenomenon may be due to the variation of crystal phase, exposed facets change and size-dependent shift. Since the crystal facet with different orientations has different electronic and surface atomic structures, the Raman spectra can be significantly influenced. The Raman spectra have been observed to be blue shifted and broadened with decreasing particle size by many researchers.^{33,34} In summary, the variation of morphology and crystal phase of tungsten oxide hierarchical nanostructures controlled by urea are fully confirmed by XPS spectra and Raman spectra.

3.2 The growth mechanism of tungsten oxides hierarchical nanostructures.

In order to deepen our understanding of the growth mechanism of hierarchical nanostructures, we studied the hierarchical nanostructures formation process by SEM. Fig. 7a-7c are the growth process of urchin-like microspheres (WU4). From Fig. 7a, it is observed that some wrinkled ultrathin nanosheets have been deposited from the solution after 30 min, suggesting that the product probably has a layered structure. In addition, from the enlarged pictures of Fig. 7b, it is observed that the nanosheets are decomposed into small particles. Fig. 7c shows some big cluster consisted with several microspheres which aggregate numerous much smaller particles (the inset in Fig. 7c) after hydrothermal reaction for 45 min. Also the trend of the cluster differentiating into several small microspheres can be clearly observed and at the differentiation site short nanowires appear. From XRD patterns shown in Fig. 7d, it is found that the samples present the same phase independent of the hydrothermal reaction time. Meanwhile, in order to elucidate the growth process of WO_3 hierarchical nanostructures assembled with 1D nanoblock, pH values of the supernatants were also recorded during the hydrothermal reaction as shown in Table S1 and Fig. 8. As for the sample (WU0) without adding urea, the pH value maintains almost the same value during the reaction. When we added 0.072 g urea in the hydrothermal precursor solution, the pH value has a slightly obvious increase from 0.7 to 1.08. Impressively, if 0.18 g urea was added, the pH value changes remarkably after reaction for 35 min until rising to 6.77 at 60 min. After reaction for 60 min, the pH values for all the solutions remain almost unchanged even if prolonging the reaction time to 12h. Meanwhile, the three samples exhibit similar morphology with final products (12 h) after reaction for 60 min as shown in Fig. S2b-

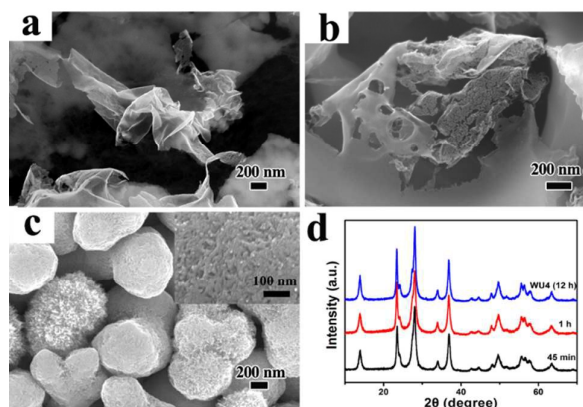
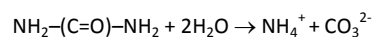


Fig. 7 SEM images of WU4 obtained at different reaction times: (a) after reacting 30 min and (b) corresponding enlarged images; (c) after reacting 45 min and corresponding enlarged images (inset); (d) XRD patterns of WU4 obtained at different reacting times.

S2d. Therefore, it could be confirmed that the morphology and phase of the products are decided in the original 1 h of the hydrothermal reaction and they are determined by the amount of urea.

The observation of layered structure tungsten trioxide hydrate is consistent with previous research.³⁵ The wrinkled ultrathin nanosheets are not obviously observed in the sample WU0 (Fig. S2a), suggesting that urea has an effect of delaminating the layered structure. Many reports found that urea tended to form 1D hydrogen-bonded chains by employing their two NH proton donors and the C=O proton acceptor in bifurcated hydrogen bonds,³⁶ which was supposed to induce the formation of 1D tungsten oxide based on this theory.³⁷ In addition, it was also demonstrated that urea enter the interlayer space forming strong hydrogen bonds.³⁸ However, it seems that during our hydrothermal reaction in $180\text{ }^\circ\text{C}$ urea was more inclined to hydrolysis thus lose its two amino groups and carbonyl since urea is a very weak Brønsted base ($\text{pK}_b \sim 13.8$), highly soluble in water, and its decomposition gives rise to ammonium carbonate:³⁹



Based on the above analysis, it is inferred that urea could insert into the interlamination of negative charged tungsten trioxide hydrate to form hydrogen-bond during the early stage ($t < 30\text{ min}$). When prolonging the reaction time, the urea no longer maintains its structure and begin to hydrolyze because of the existence of abundant water at high temperature. Due to the hydrolysis, the interlayer water are consumed leading to the exfoliation of $\text{WO}_3 \cdot n\text{H}_2\text{O}$ hydrates precursor sheets which has the similar effect in preparing LDHs.⁴⁰ Then the thin nanosheets are unstable in the hydrothermal solution and begin to decompose into small nucleus. Weak Bronzed basic urea hydrolyses to release ammonium or OH^- in a certain time, leading to high pH value. This is especially significant for forming ultrathin $h\text{-WO}_3$ nanobelts. At early stage ($t < 30\text{ min}$) the hydrolysis of urea has not fully started, it can play the role of intercalation. At about 35 min, the pH value is still low ($\text{pH} < 1$) ensuring nucleate successfully since WO_3 is not stable in alkaline environment. The urea begin to hydrolyse violently due to the high temperature and pressure, resulting in a high pH value.

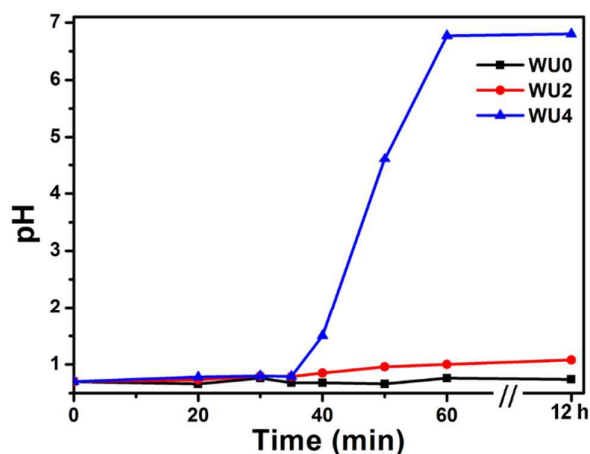


Fig. 8 pH variations of supernatants during the hydrothermal reaction to prepare WU0, WU2 and WU4

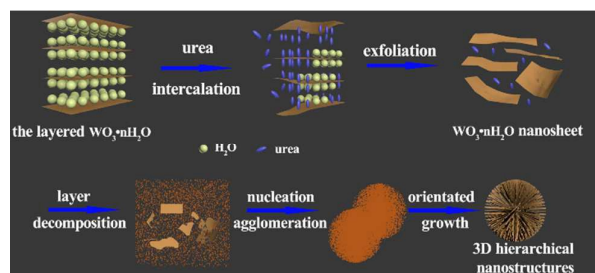


Fig. 9 Schematic illustration of the formation mechanism of tungsten oxides hierarchical nanostructures

In the weakly acidic environment, ammonium can selectively adsorb on certain facets, and hence the nanobelts can form and maintain until the ending of the reaction. Therefore, high pH value results in a h - WO_3 phase with ultrathin nanobelt, otherwise, it will cause the formation of o - $WO_3 \cdot 0.33H_2O$. That is to say the concentration of urea is significant for controlling the phase and exposed facets for tungsten oxide: high concentration of urea enables the nanosheets to be exfoliated completely and the water molecules between these nanosheets to be removed entirely, thus forming ultra-small nuclei of tungsten oxide without water

molecules, otherwise, o - $WO_3 \cdot 0.33H_2O$ with thick nanorods will appear. To sum up, adjusting the concentration of urea to achieve a proper pH value, the sample with controllable phase and exposed facets can be obtained. The whole formation mechanism of tungsten oxides hierarchical nanostructures is proposed as illustrated in Fig. 9.

3.3 Photocatalytic activity

The visible-light-driven photocatalytic activities of the h - WO_3 and o - $WO_3 \cdot 0.33H_2O$ prepared by adjusting the amount of urea in the hydrothermal precursor solution were measured by decoloring RhB solution. As shown in Fig. 10a, in the absence of photocatalyst, the optical absorption of RhB shows no obvious change, suggesting there is no obvious degradation of RhB without photocatalyst. Only 48.4% of RhB can be photodegraded by WU0 in 100 min, while the photodegradation rate of RhB by WU3 is 94.2% at the same time. Meanwhile, the linear relationship between $\ln(C_0/C)$ and t indicates that the photodegradation reactions follow pseudo-first-order kinetics (see Fig. 10b) with rate constants 0.0066, 0.0106, 0.0272, 0.0254 and 0.0131 min^{-1} for WU0, WU1, WU2, WU3 and WU4. All the samples display higher performance in degrading RhB than WU0. Moreover, as for the samples with o - $WO_3 \cdot 0.33H_2O$ phase, the photocatalytic performance is enhancing with increasing the amount of urea and WU3 presents the highest photocatalytic activity among all the samples which is 4.1 times as high as the sample obtained without using urea. However, sample WU4 with specific surface area about three times higher than WU3 and WU2 shows lower photocatalytic activity, which is perhaps due to their different crystal phases and exposed facets. Meanwhile, o - $WO_3 \cdot 0.33H_2O$ (WU3) also maintains high photocatalytic activity until 4 recycling experiments.

The exposed facets have a significant effect on photocatalytic performance, because both electronic and surface atomic structures sensitively depend on the crystal facet of the photocatalyst.^{21, 22, 41, 42} The o - $WO_3 \cdot 0.33H_2O$ crystals prepared by hydrothermal reaction experience the evolution of crystal planes as the concentration of urea increases. As the mass of urea increases, the morphology of the samples evolves from nanobrick (WU1:0.036 g) to nanorod (WU2: 0.072 g) and then to nanoflake (WU3:0.144 g)

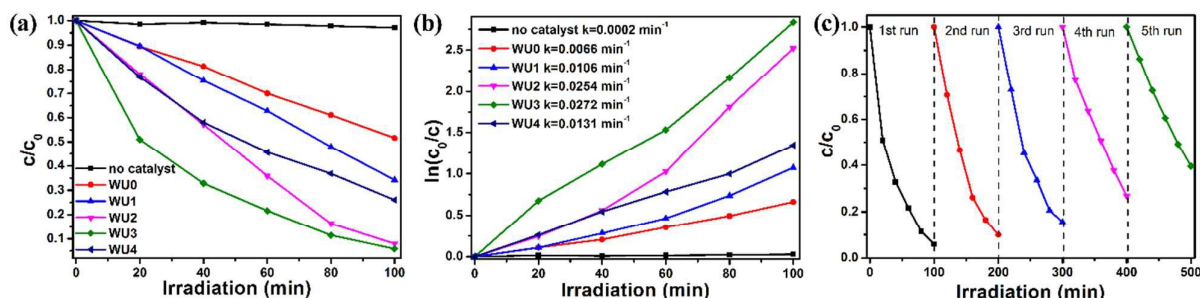


Fig. 10 Concentration change of RhB solution versus irradiation time (a) and pseudo-first-order linear fitting results (κ , apparent kinetic rate constant) (b) decolorized by the samples prepared by adding different mass of urea (WU0, WU1, WU2, WU3 and WU4); (c) recyclability of the photocatalytic decomposition of RhB by o - $WO_3 \cdot 0.33H_2O$ (WU3).

with increasing (020) facet (see Fig. 5). Moreover, it reveals that WU1, WU2 and WU3 (18.2, 20.6 and 21.45 m^2g^{-1}) have close specific surface area but with obviously different photocatalytic performance following the order $\text{WU3} > \text{WU2} > \text{WU1}$, demonstrating (020) facet is the active facet for $\text{o-WO}_3 \cdot 0.33\text{H}_2\text{O}$. It is observed that the building block of h-WO_3 hierarchical nanostructure prepared by adding high concentration urea exposes almost all (020) facet, suggesting that (020) may not be the active facet of h-WO_3 for degrading RhB. Besides, adsorption ability is also related to different exposed facets and the adsorption experiments in the dark demonstrate the accessibility of the surfaces of the photocatalyst.⁴³ It was reported that there were $\text{W}=\text{O}$ and $\text{O}-\text{H}$ groups in $\text{o-WO}_3 \cdot 0.33\text{H}_2\text{O}$ which not only facilitated superior adsorption of polar compounds such as RhB but also increased the hydrophilicity of $\text{o-WO}_3 \cdot 0.33\text{H}_2\text{O}$.⁴⁴ Sample WU3 with $\text{o-WO}_3 \cdot 0.33\text{H}_2\text{O}$ phase and exposing most (020) facet exhibits excellent adsorption ability (Fig. 11), which results in highest performance, while WU4 with h-WO_3 phase shows a decreased adsorption ability. The exposed facet (020) is highly active for $\text{o-WO}_3 \cdot 0.33\text{H}_2\text{O}$ phase but not for h-WO_3 , thus $\text{o-WO}_3 \cdot 0.33\text{H}_2\text{O}$ performs better than h-WO_3 .

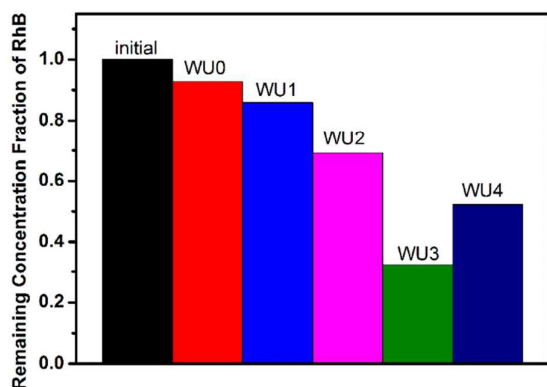


Fig. 11 Adsorption ability of samples prepared by different amount of urea (adsorption experiments were carried out with stirring overnight in dark)

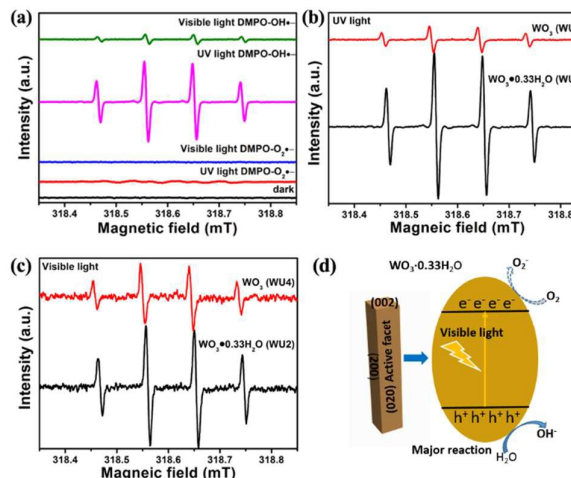


Fig. 12 ESR spectra of radical adduct trapped (a) by DMPO ($\text{DMPO-O}_2\bullet^-$) over the sample $\text{o-WO}_3 \cdot 0.33\text{H}_2\text{O}$ (WU2) in the methanol solution and DMPO ($\text{DMPO-OH}\bullet$) over the same sample in aqueous solution with the visible light irradiation or UV irradiation or without light irradiation; DMPO ($\text{DMPO-OH}\bullet$) over the sample $\text{o-WO}_3 \cdot 0.33\text{H}_2\text{O}$ (WU2) and h-WO_3 (WU4) in aqueous solution with UV irradiation (b) or visible light irradiation (c); (d) schematic illustration of photocatalytic mechanism.

In order to further explore the photocatalytic mechanism and the cause of performance enhancement of the samples, the electron paramagnetic resonance spectroscopy (ESR) was measured to detect the reactive species during photocatalysis, as shown in Fig. 12. For the sample $\text{o-WO}_3 \cdot 0.33\text{H}_2\text{O}$ (see Fig. 12a), no signal is observed in the dark and a quartet signal characteristic of the $\text{DMPO-OH}\bullet$ adduct with an intensity of 1:2:2:1 is observed under visible light and UV light irradiation. Besides, the signal under UV light irradiation is much stronger than that under the visible light. However, the single-electron reduction of O_2 to superoxide radicals ($\text{O}_2\bullet^-$) is not feasible by the present sample, suggesting that hydroxyl radicals ($\text{OH}\bullet$) play the major role in degrading the RhB. Besides, the signal of $\text{DMPO-OH}\bullet$ achieved by $\text{o-WO}_3 \cdot 0.33\text{H}_2\text{O}$ is much stronger than that by h-WO_3 under UV light or visible light irradiation (see Fig. 12b-c), which is consistent with the rule of photocatalytic performance shown in Fig. 10. To sum up, the main radical responsible for the decomposition of RhB is hydroxyl radicals and the photocatalytic mechanism of tungsten oxides hierarchical nanostructures is proposed as illustrated in Fig. 12d.

Based on the above considerations, it can be concluded that crystalline phase and exposed facets all can affect the photocatalytic activity. For tungsten oxides, $\text{o-WO}_3 \cdot 0.33\text{H}_2\text{O}$ and h-WO_3 have different active facets. $\text{WO}_3 \cdot 0.33\text{H}_2\text{O}$ with $\text{W}=\text{O}$ and $\text{O}-\text{H}$

groups exhibiting excellent adsorption and exposing the most active (020) facet achieve high photocatalytic activities.

4. Conclusion

In summary, we report the controllable fabrication of tungsten oxides architectures assembled with different 1D nanosized building blocks by assisting of urea via hydrothermal reaction. It is found that building blocks variation from nanobricks via nanorods and nanoflakes and finally to nanobelts corresponds to the exposed facets variation from (200), (020), (002) to (020). Moreover, tungsten oxide could transform from $\alpha\text{-WO}_3 \cdot 0.33\text{H}_2\text{O}$ to $\beta\text{-WO}_3$ and shows an increasing percentage of (020) facet by controlling the amount of urea. Two NH proton donors and the C=O proton acceptor enable urea to insert into the layers of tungsten oxide hydrates and its nature of weak base allows it to cause the change of pH value during hydrothermal reaction through hydrolysis, thereby realizing both phase-control and exposed facets-control since the amount of urea affect its hydrolysis degree and the delamination effect. Meanwhile, it was found that (020) is the active facet of $\alpha\text{-WO}_3 \cdot 0.33\text{H}_2\text{O}$ but not for $\beta\text{-WO}_3$. The as-prepared sample belonging to an $\alpha\text{-WO}_3 \cdot 0.33\text{H}_2\text{O}$ with exposing most (020) facets shows high photocatalytic activity for the degradation of RhB under visible light illumination.

Acknowledgements

This work was supported by the National Basic Research Program of China (973 Program) (No. 2013CB934301) and the National Science Foundation of China (Grant No. 91222110 and 51472013).

Notes and references

^a State Key Laboratory of New Ceramics and Fine Processing, School of Materials Science and Engineering, Tsinghua University, Beijing 100084, China

^b Department of Physics, Beihang University, Beijing 100191, China

*E-mail address: tzl@tsinghua.edu.cn; zjy@buaa.edu.cn; Tel: +86 10 62783685; Fax: +86 10 62771160

† Electronic Supplementary Information (ESI) available. See DOI: 10.1039/b000000x/

- X. Liu, F. Y. Wang and Q. Wang, *Phys. Chem. Chem. Phys.*, 2012, **14**, 7894-7911.
- H. Tong, S. Ouyang, Y. Bi, N. Umezawa, M. Oshikiri and J. Ye, *Adv. Mater.*, 2012, **24**, 229-251.
- S. Pany and K. M. Parida, *ACS Sustain. Chem. Eng.*, 2014, **2**, 1429-1438.
- C. L. Yu, K. Yang, Y. Xie, Q. Z. Fan, J. C. Yu, Q. Shu and C. Y. Wang, *Nanoscale*, 2013, **5**, 2142-2151.
- C. L. Yu, J. C. Yu and M. Chan, *J. Solid State Chem.*, 2009, **182**, 1061-1069.
- L. Ye, J. Mao, J. Liu, Z. Jiang, T. Peng and L. Zan, *J. Mater. Chem. A*, 2013, **1**, 10532-10537.
- N. Roy, Y. Sohn and D. Pradhan, *ACS Nano*, 2013, **7**, 2532-2540.
- J. Biedrzycki, S. Livraghi, E. Giamello, S. Agnoli and G. Granozzi, *J. Phys. Chem. C*, 2014, **118**, 8462-8473.
- W. Q. Fang, Z. Y. Huo, P. R. Liu, X. L. Wang, M. Zhang, Y. Jia, H. M. Zhang, H. J. Zhao, H. G. Yang and X. D. Yao, *Chem-Eur. J.*, 2014, **20**, 11439-11444.
- D. Xu, T. Jiang, D. Wang, L. Chen, L. Zhang, Z. Fu, L. Wang and T. Xie, *ACS Appl. Mater. Interfaces*, 2014, **6**, 9321-9327.
- X. He, C. Hu, Y. Xi, K. Zhang and H. Hu, *Mater. Res. Bull.*, 2014, **50**, 91-94.
- C. L. Yu, F. F. Cao, X. Li, G. Li, Y. Xie, J. C. Yu, Q. Shu, Q. Z. Fan and J. C. Chen, *Chem. Eng. J.*, 2013, **219**, 86-95.
- W. Ong, L. Tan, S. Chai, S. Yong and A. R. Mohamed, A. R., *ChemSusChem*, 2014, **7**, 690-719.
- L. Liu, Z. Liu, A. Liu, X. Gu, C. Ge, F. Gao and L. Dong, *ChemSusChem*, 2014, **7**, 618-626.
- X. Duan, D. Li, H. Zhang, J. Ma and W. Zheng, *Chem. Eur. J.*, 2013, **19**, 7231-7242.
- M. Yao, Q. Li, G. Hou, C. Lu, B. Cheng, K. Wu, G. Xu, F. Yuan and Y. Chen, *ACS Appl. Mater. Interfaces*, 2015, **7**, 2856-2866.
- H. Zhang, M. Yao, L. Bai, W. Xiang, H. Jin, J. Li and F. Yuan, *CrystEngComm*, 2013, **15**, 1432-1438.
- Z. Zhao, Z. Liu and M. Miyauchi, *Chem. Commun.*, 2010, **46**, 3321-3323.
- Y. Guo, X. Quan, N. Lu, H. Zhao and S. Chen, *Environ. Sci. Technol.*, 2007, **41**, 4422-4427.
- H. G. Yang, C. H. Sun, S. Z. Qiao, J. Zou, G. Liu, S. C. Smith, H. M. Cheng and G. Q. Lu, *Nature*, 2008, **453**, 634-638.
- Y. P. Xie, G. Liu, L. Yin and H. Cheng, *J. Mater. Chem.*, 2012, **22**, 6746-6751.
- M. D'Arenzo, L. Armelao, C. M. Mari, S. Polizzi, R. Ruffo, R. Scotti and F. Morazzoni, *RSC Adv.* 2014, **4**, 11012-11022.
- G. Li, T. Varga, P. Yan, Z. Wang, C. Wang, S. A. Chambers and Y. Du, *Phys. Chem. Chem. Phys.*, 2015, **17**, 15119-15123.
- J. Y. Zheng, G. Song, J. Hong, K. V. Thanh, A. U. Pawar, D. Y. Kim, C. W. Kim, Z. Haider and Y. S. Kang, *Cryst. Growth Des.*, 2014, **14**, 6057-6066.
- J. Li, J. Huang, J. Wu, L. Cao, Q. Li and K. Yanagisawa, *CrystEngComm*, 2013, **15**, 7904-7913.
- J. Y. Zheng, Z. Haider, T. K. Van, A. U. Pawar, M. J. Kang, C. W. Kim and Y. S. Kang, *CrystEngComm*, 2015, **17**, 6070-6093.
- Q. Q. Jia, H. M. Ji, D. H. Wang, X. Bai, X. H. Sun and Z. G. Jin, *J. Mater. Chem. A*, 2014, **2**, 13602-13611.
- J. A. Zhu, S. L. Wang, S. H. Xie and H. X. Li, *Chem. Commun.*, 2011, **47**, 4403-4405.
- X. G. Han, X. Han, L. Li and C. Wang, *New J. Chem.*, 2012, **36**, 2205-2208.
- S. Peters, S. Peredkov, M. Al-Hada, M. Neeb and W. Eberhardt, *J. Electron. Spectrosc.*, 2014, **192**, 52-54.
- Y. Busby and J. J. Pireaux, *J. Electron. Spectrosc.*, 2014, **192**, 13-18.
- A. I. Kovalev, D. L. Wainstein, A. Y. Rashkovskiy, A. Osheroov and Y. Golan, *Surf. Interface Anal.*, 2010, **42**, 850-854.
- Y. N. Hwang, S. H. Park and D. Kim, *Phys. Rev. B*, 1999, **59**, 7285-7288.
- C. I. Vargas-Consuelos, K. Seo, M. Camacho-Lopez and O. A. Graeve, *J. Phys. Chem. C*, 2014, **118**, 9531-9537.
- J. Livage and G. Guzman, *Solid State Ionics*, 1996, **84**, 205-211.
- R. Custelcean, *Chem. Commun.*, 2008, **3**, 295-307.
- Z. Zhao and M. Miyauchi, *J. Phys. Chem. C*, 2009, **113**, 6539-6546.
- E. Mako, J. Kristof, E. Horvath and V. Vagvolgyi, *J. Colloid Interf. Sci.*, 2009, **330**, 367-373.
- M. Adachi-Pagano, C. Forano and J. P. Besse, *J. Mater. Chem.*, 2003, **13**, 1988-1993.
- Y. Wei, F. Li and L. Liu, *RSC Adv.*, 2014, **4**, 18044-18051.
- J. Shi, G. Hu, R. Cong, H. Bu and N. Dai, *New J. Chem.*, 2013, **37**, 1538-1544.
- L. Zhou, J. Zou, M. M. Yu, P. Lu, J. Wei, Y. Q. Qian, Y. H. Wang and C. Z. Yu, *Cryst. Growth Des.*, 2008, **8**, 3993-3998.
- M. S. Bazarjani, M. Hojamberdiev, K. Morita, G. Zhu, G. Cherkashinin, C. Fasel, T. Herrmann, H. Breitzke, A. Gurlo and R. Riedel, *J. Am. Chem. Soc.*, 2013, **135**, 4467-4475.
- B. Liu, J. Wang, J. Wu, H. Li, Z. Li, M. Zhou and T. Zuo, *J. Mater. Chem. A*, 2014, **2**, 1947-1954.